

# Grain shape of basaltic ash populations: implications for fragmentation

Johanne Schmith<sup>1,2</sup> · Ármann Höskuldsson<sup>1</sup> · Paul Martin Holm<sup>2</sup>

Received: 17 January 2016 / Accepted: 13 December 2016 / Published online: 24 January 2017  
© Springer-Verlag Berlin Heidelberg 2017

**Abstract** Here, we introduce a new quantitative method to produce grain shape data of bulk samples of volcanic ash, and we correlate the bulk average grain shape with magma fragmentation mechanisms. The method is based on automatic shape analysis of 2D projection ash grains in the size range 125–63  $\mu\text{m}$ . Loose bulk samples from the deposits of six different basaltic eruptions were analyzed, and 20,000 shape measurements for each were obtained within  $\sim 45$  min using the Particle Insight<sup>TM</sup> dynamic shape analyzer (PIdsa). We used principal component analysis on a reference grain dataset to show that circularity, rectangularity, form factor, and elongation best discriminate between the grain shapes when combined. The grain population data show that the studied eruptive environments produce nearly the same range of grain shapes, although to different extents. Our new shape index (the regularity index (RI)) places an eruption on a spectrum between phreatomagmatic and dry magmatic fragmentation. Almost vesicle-free Surtseyan ash has an RI of  $0.207 \pm 0.002$  ( $2\sigma$ ), whereas vesiculated Hawaiian ash has an RI of  $0.134 \pm 0.001$  ( $2\sigma$ ). These two samples define the end-member RI, while two subglacial, one lacustrine, and another

submarine ash sample show intermediate RIs of  $0.168 \pm 0.002$  ( $2\sigma$ ),  $0.175 \pm 0.002$  ( $2\sigma$ ),  $0.187 \pm 0.002$  ( $2\sigma$ ), and  $0.191 \pm 0.002$  ( $2\sigma$ ), respectively. The systematic change in RI between wet and dry eruptions suggests that the RI can be used to assess the relative roles of magmatic vs. phreatomagmatic fragmentation. We infer that both magmatic and phreatomagmatic fragmentation processes played a role in the subglacial eruptions.

**Keywords** Explosive · Basaltic · Ash · Tephra · Grain · Morphology · Fragmentation · Iceland

## Introduction

Hazard evaluations of explosive eruptions are often based on information extracted from the geological tephra record. The significant differences between the hazards posed by magmatic and phreatomagmatic eruptions of basaltic magmas (e.g., Nemeth and Cronin 2011) mean that fragmentation is a key parameter, which is routinely studied on the basis of tephra grain morphology (e.g., Murtagh and White 2013; Dellino et al. 2012; Graettinger et al. 2013; Cioni et al. 2014; Miwa et al. 2015). To obtain interpreter-independent results, most methods are based on quantitative analysis of grain morphology (e.g., Leibrandt and Le Pennec 2015; Liu et al. 2015a; Genareau et al. 2013; Proussevitch et al. 2011; Büttner et al. 2002; Maria and Carey 2002), but current fragmentation classification methods cannot match observations of complex fragmentation events (e.g., Graettinger et al. 2013; Jordan et al. 2014). Therefore, we have developed a new quantitative method for studying the fragmentation processes of basaltic tephra deposits. It automates shape parameterization for ash in the size-range 125–63  $\mu\text{m}$  for small samples with good reproducibility. The classification diagram models only the

---

Editorial responsibility: R.J. Brown

**Electronic supplementary material** The online version of this article (doi:10.1007/s00445-016-1093-5) contains supplementary material, which is available to authorized users.

✉ Johanne Schmith  
johasch@hi.is

<sup>1</sup> Nordic Volcanological Center, Earth Science Institute, University of Iceland, Reykjavik, Iceland

<sup>2</sup> Department of Geosciences and Natural Resource Management, University of Copenhagen, Copenhagen, Denmark

particles actively involved in the explosion and provides a quantitative spectrum between magmatic and phreatomagmatic fragmentation to allow for a more complex fragmentation evaluation.

### Background of grain morphology and fragmentation

Tephra grain morphology has been linked to magma fragmentation by two different approaches. One is volcanological and combines grain morphology with eruption types and volcanic processes. It distinguishes between magma fragmentation by either magmatic volatile exsolution (magmatic) or by explosive interaction with external water (phreatomagmatic), thus focusing on fragmentation drivers (e.g., Heiken 1972; Dellino et al. 2012; Murtagh and White 2013). The other approach is mechanical and describes magma fragmentation in fluid dynamic terms as either brittle or ductile deformation (e.g., Büttner et al. 2002; Dürig et al. 2012). The volcanological approach is typically used in studies of field samples of tephra, while fluid dynamic approaches are often preferred in experimental studies.

### The volcanological morphology framework

The systematic features that link tephra morphology to eruption types were based on overall grain shape and surface features derived from SEM imagery (Heiken 1972). For the magmatic fragmentation scheme, it characterized ash from fire fountains as whole smooth-skinned rounded droplets, elongated strands (Pele's hairs), and broken, ragged, and irregular droplets (Heiken 1972). For magmatic Strombolian activity, Heiken (1972) noted equant grains, which contained ovoid to spherical vesicles.

Another classification ties grain morphology to the magmatic volatile exsolution processes by defining simple and complex particles (Prousevitch et al. 2011). Simple ash particles have full-length curved sides representing bubble walls and represent the plateau border between three or more bubbles. Complex particles have indents from more bubbles on their surface and result from the breakage of larger bubbles. Complex particles are larger than the simple particles and for proximal basaltic samples they range in size from 50  $\mu\text{m}$  and up (Genareau et al. 2013), while simple particles dominate the finer ash.

Phreatomagmatic eruptions produce blocky, mostly equant, grains with planar to curvi-planar faces, smooth or stepped surfaces, and faces meeting at nearly right angles (Heiken 1972; Wohletz 1983; Büttner et al. 2002). Vesicles are scarce and usually spherical (Heiken 1972, 1974). Other characteristic morphology traits include moss-like and platy textures, which are usually found in grains smaller than 63  $\mu\text{m}$  (Wohletz 1983).

Graettinger et al. (2013) showed that magmatic gas-driven explosions could trigger phreatomagmatic ones and vice versa creating feedback loops between these two fragmentation types. This explosion facilitation creates highly complex deposits, which can be difficult to interpret in terms of a main fragmentation process (Jordan et al. 2014), though volcanological morphology studies of ash still characterizes deposits as either magmatic or phreatomagmatic (e.g., Murtagh and White 2013; Jordan et al. 2014).

### The fluid dynamic morphology framework

This experimental perspective highlights the important distinction between passive and active particle formation (Zimanowski et al. 1997a; Büttner et al. 2002; Dürig et al. 2012). Active particles are produced directly in the explosion whereas passive particles are not. Molten fuel-coolant interaction (MFCI) experiments show that the active particles are angular (blocky) and crack-dominated particles less than 130  $\mu\text{m}$  in size related to brittle fragmentation (Zimanowski et al. 1997a; Büttner et al. 2002). Passive particles are related to ductile fragmentation and consist of spherical and elongated drops and broken strands (Zimanowski et al. 1997a).

### Connecting volcanological and experimental data

Phreatomagmatic eruption deposits have been associated with blocky grains inferred to represent the active MFCI particles (Wohletz 1983; Zimaowski et al. 1997a), but blocky particles can also be formed passively by quench granulation in a non-explosive interaction with water. Quench granulation is caused by brittle failure of the material as it contracts during cooling and produces grain sizes around coarse ash to fine lapilli (Mastin et al. 2009; Schipper et al. 2011b; Graettinger et al. 2013). Furthermore, natural brittle fragmentation involves fragmentation of prestressed material (Dürig et al. 2012) and cannot solely be attributed to MFCI.

Passive particles are placed in the magmatic morphology scheme although they are also created in MFCI explosions (Zimanowski et al. 1997a; Wohletz 1983). Thus, active and passive particle classes cannot be directly equated to volcanological morphology suites.

For hazard assessment purposes, the active particles generated by the explosion are the important ones. Therefore drops, hairs, and blocky passive shapes should be removed from the dataset, as they are passive particles. The data of Genareau et al. (2013), Graettinger et al. (2013), Büttner et al. (2002), and Wohletz (1983) suggests that the optimal size interval of volcanic ash particles for studying active eruption fragmentation is between 3 and 4  $\varphi$  (125–63  $\mu\text{m}$ ).

## Method background

### Automatic shape analysis

Interpretation of qualitative grain morphology is largely subjective and interpreter dependent (Sheridan and Marshall 1983) and therefore quantitative shape parameters were developed to remove interpreter bias. Leibrandt and Le Pennec (2015) and Liu et al. (2015a) have given extensive reviews of both the history and nomenclature of shape parameters and only highlights will be repeated here.

Dellino and LaVolpe (1996) used image parameter analysis (IPA) and constructed four dimensionless parameters, which were assigned to the 2D projection of the selected tephra particles on photographs and SEM images by automated image analysis software. Using multivariate data analysis, the four parameters were combined to a 2D diagram to distinguish between ductile and brittle fragmentation (passive and active particles) (Buttner et al. 2002). Murtagh and White (2013) added a magmatic/phreatomagmatic fragmentation regime boundary to the diagram.

The IPA shape parameters relate to properties of the tephra particle as a whole such as length/width, area, and perimeter. These metrics are measured in raster-based imagery-counting pixels. To obtain stable bulk average results, around 1000–1500 particles should be analyzed per sample (Leibrandt and Le Pennec 2015). The shape parameters are more or less sensitive to image sharpness, resolution, and pixel classification model. The least-sensitive parameters are area and length, which receive the largest contribution from the unambiguous pixels within the grain and converge towards a single best estimate value with increasing resolution. Liu et al. (2015a) have found a minimum resolution of 750 pixels/particle to get stable area and length parameters. Perimeter, however, is calculated from ambiguous edge pixels and thus highly resolution and pixel-smoothing dependent. Perimeter values of tephra increase with increased resolution (Maria and Carey 2002), which suggests a fractal/pseudo-fractal behavior of the perimeter (e.g., Dellino and Liotino 2002; Maria and Carey 2002). This is used in the fractal method of morphology classification (e.g., Dellino and Liotino 2002; Maria and Carey 2002, 2007; Perugini and Kueppers 2012), but the method has not yet been automated for large grain capacities.

3D shape analysis is yet another branch of morphology studies currently being developed with promising results, but it remains laborious, costly, and can only produce data on a few grains at this stage (Bagheri et al. 2015).

Thus the 2D projection method remains the fastest, most cost effective, and widely used (Leibrandt and Le Pennec 2015).

### The IPA shape parameters

To aid interpretation, 2D particle metrics are mostly described by geometric shapes; i.e., circles, rectangles, ellipses, or polygons. Directly constructed grain geometries include circumscribing circles, ellipses, rectangles, or polygons. A group of model geometries translates some of the particle properties (length, width, area, or perimeter) into simple shape models by constructing, for example, a circle with the same area or perimeter as the grain. The geometric shapes are intuitive to interpret and to compare with the measured particle metrics by the IPA parameter formulas (Table 1). To be able to compare different grain sizes, IPA parameters are often constructed to be dimensionless and some have values between 0 and 1.


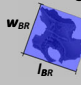
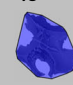



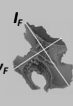




Unfortunately, due to differences in software and nomenclature in the literature, 2D shape parameters have no standard reference. Parameters with the same name can be defined differently in different studies and conversely parameters calculated in the same way may bear different names across different publications. The nomenclature in this paper follows the Pidsa software, but otherwise following Liu et al. (2015a).

### Connecting tephra morphology and shape parameters

Complex tephra grain morphology cannot be uniquely captured by one single shape parameter (Liu et al. 2015a). Instead, it can be divided into three main types of shape variation, which are captured by different groups of shape parameters (Liu et al. 2015a). One group deals with the dimensions of the grain in terms of elongation expressed as aspect ratio. Another group (the morphology roughness of Liu et al. 2015a) deals with the overall geometric shape of the grain seen as either larger bubble walls or straight breakage faces defining the outline of the tephra grain. It is best evaluated by comparing the area of the particle with the area of a model geometric shape (circle, ellipse, rectangle, or convex hull). The last group (textural roughness of Liu et al. 2015a) deals with surface perturbations, such as small vesicles or breaking steps on the grain surface that do not change the overall geometry and is measured by perimeter parameters.

Tephra morphology can then be described by using a parameter from each group; elongation, morphology roughness, and textural roughness. However, elongation and morphology roughness are determined from length and area measures, which are stable in high-resolution raster imagery, but textural roughness is perimeter derived and is thus dependent on sharpness and resolution (Leibrandt and Le Pennec 2015). The specific choice of parameters depends on the analytical settings, software output, particle orientation, and resolution and should always be considered carefully for each experimental setup.

**Table 1** Shape parameter overview and definitions from the PIdsa

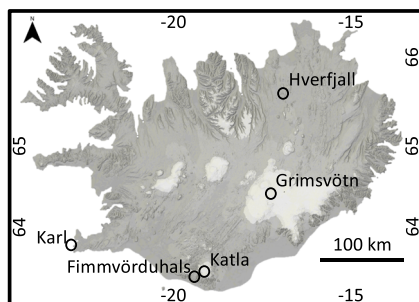
Circle model	Rectangle model	Polygon model	Other parameters
<b>Equivalent area circle diameter</b>  $d_{EAC} = \sqrt{\frac{A_p}{\pi} \cdot 4}$	<b>Bounding Rectangle length &amp; width</b>  $l_{BR} \text{ \& } w_{BR} \text{ are the length and width of the smallest area rectangle that encloses, but does not intersect the particle}$	<b>Polygon order</b>  <p>Number of sides in a convex polygon fitted to the particle</p>	<b>Particle measures</b> $A_p$ = Area of particle $P_p$ = Perimeter of particle $r_p$ = Radius of particle
<b>Equivalent perimeter circle diameter</b>  $d_{EPC} = \frac{P_p}{\pi}$	<b>Bounding Rectangle aspect ratio</b> $AR_{BR} = \frac{l_{BR}}{w_{BR}}$	<b>Convexity</b>  $CV_{CP} = \frac{A_p}{A_{CP}}$	<b>Model measures</b> $A_{CP}$ = Area of convex polygon
<b>Bounding Circle Diameter</b>  <p><math>d_{BC}</math> = Diameter of the smallest circle that encloses, but does not intersect the particle</p>	<b>Rectangularity</b> $R = \frac{A_p}{l_{BR} \cdot w_{BR}}$	<b>Irregular model</b> <b>Feret length &amp; width (caliper dimensions)</b>  <p><math>l_f</math> = Smallest distance between two parallel lines that contact but do not intersect the particle  <math>w_f</math> = Largest distance between two parallel lines orthogonal to <math>l_f</math> that contact but do not intersect the particle</p>	<b>Dellino and LaVolpe 1996</b> <b>Circularity</b> $C_{DLV} = \frac{P_p}{2\pi^{0.5} A_p^{0.5}}$
<b>Mean Radius Diameter</b>  <p><math>d_{MR} = \bar{r}_p \cdot 2</math>                      Particle radius from centroid to perimeter measured at 36 equally spaced angles</p>	<b>Ellipse model</b> <b>Equivalent elliptic area length &amp; width</b>  $l_{EEA} = 2 \sqrt{\frac{A_p \cdot AR_{BR}}{\pi}}$ $w_{EEA} = 2 \sqrt{\frac{A_p}{\pi \cdot AR_{BR}}}$	<b>Feret aspect ratio</b> $AR_F = \frac{l_F}{w_F}$	<b>Elongation</b> $E_{DLV} = \frac{\text{max intercept}}{\text{mean intercept perpendicular}}$
<b>Circularity</b> $C = \frac{4A_p}{\pi d_{BC}^2}$	<b>Ellipse aspect ratio</b> $AR_{EEA} = \frac{l_{EEA}}{w_{EEA}} = \frac{l_{BR}}{w_{BR}}$	<b>Fiber model</b> <b>Fiber length &amp; width</b>  $D = \frac{P_p^2 - 16A_p}{4}, \text{ If } D > 0 \text{ then}$ $l_{FB} = \frac{P_p + 2\sqrt{D}}{4}$ $w_{FB} = \frac{A_p}{l_{FB}}$	<b>Compactness = R</b> <b>Rectangularity</b> $R_{DLV} = \frac{P_p}{2l_{BR} + 2w_{BR}}$
<b>Form Factor</b> $FF = \frac{4\pi A_p}{P_p^2}$	<b>Bounding ellipse length and width</b>  <p><math>l_{BE}</math> &amp; <math>w_{BE}</math> = length and width of the smallest area ellipse that encloses, but does not intersect the particle</p>	<b>Fiber aspect ratio</b> $AR_{FB} = \frac{l_{FB}}{w_{FB}}$	<b>Leibrandt and LePenneec 2015</b> <b>Circularity</b> $C_{LLP} = \frac{1}{C_{DLV}}$
<b>Compactness</b> $CP_C = \frac{2 \cdot \sqrt{A_p}}{\sqrt{\pi d_{BC}^2}}$	<b>Ellipsicity</b> $E_{BE} = \frac{4A_p}{\pi \cdot l_{BE} \cdot w_{BE}}$		<b>Convexity</b> $CV_{LLP} = \frac{P_{CP}}{P_p}$ $P_{CP}$ = Perimeter of convex polygon
			<b>Liu et al., 2015</b> <b>Convexity = <math>CV_{LLP}</math></b> <b>Solidity = <math>CV_{CP}</math></b> <b>Rectangularity = <math>R_{DLV}</math></b>

The 25 parameters used in this study are described by shape model and shape name, and equations are shown where relevant. See additional comments in text about shape models and parameters. Additional used parameters from other studies are shown beneath the relevant references

**Method**

**Sample selection**

Samples of five basaltic tephra fall deposits were collected from multiple different volcanic settings in Iceland (Fig. 1) and one sample site from Jan Mayen Island, Norway. Sample information is presented in Table 2. The deposits were carefully chosen to avoid samples that may have been altered by erosion or transport. The Katla and Grimsvötn tephra layers were sampled from the middle unit of a series of several consecutive fall units.



**Fig. 1** Map of Iceland showing the source locations of the sampled eruptions

The Karl sample was chosen from a cm thick fall unit in the deposit and the Hverfjall deposit was sampled on the crater rim to ensure that no flow transport had affected the grains. The tephra have similar SiO<sub>2</sub> contents ranging from 46.5 to 49.7 wt.% (Table 2) and contain only scarce phenocrysts and microlites. They are therefore ideal for comparing the tephra populations from different eruptive settings.

**Sample preparation**

Samples were dried at 50 °C and carefully hand sieved dry through a 125 μm (3 φ) and a 63 μm (4 φ) sieve. Small subsamples were mounted on carbon tape on a Hitachi 12.5 mm sample stub, were gold coated and then studied in a scanning electron microscope (SEM) to look for erosion features on the grains and get a qualitative overview of grain types (see Electronic supplementary material Fig. 1). Erosion features were not observed.

**Image analysis**

Fifty to ninety milligrams of sieved bulk sample was run on the Particle Insight™ dynamic shape analyzer (PIdsa). The

**Table 2** Overview of the six tephra fall samples used in this study

Eruption	Fimmvörðuháls 2010	Eggoya 1732	Katla 1755	Grímsvötn 2011	Hverfall 2500 BP	Karl 1210–1240
Location	Iceland	Jan Mayen, Norway	Iceland	Iceland	Iceland	Iceland
Eruption type	Hawaiian	Surtseyan	Subplinian	Subplinian	Surtseyan	Surtseyan
Vent type	Fissure	Submarine vent	Subglacial vent	Subglacial vent	Lacustrine fissure	Submarine vent
Deposit type	Loose tephra deposit	Tuff cone fall unit	Tephra layer	Tephra layer	Tuff ring	Tuff cone fall unit
Fragmentation	Dry magmatic	Phreatomagmatic	Phreatomagmatic	Phreatomagmatic	Phreatomagmatic	Phreatomagmatic
Sampling	Few 100 m from source during the eruption	~2 km from vent in costal section from second fall unit (P1–2)	~22 km from vent in soil section from fifth fall unit	~9 km from vent in glacial section from third fall unit	From crater of eruption phase III	~300 m from vent in costal section
Geochemistry	Alkali basalt 46.8 wt.% SiO <sub>2</sub>	Alkali basalt 46.5–48 wt.% SiO <sub>2</sub>	Transalkalic basalt 47.8 wt.% SiO <sub>2</sub>	Tholeiitic basalt 49.5 wt.% SiO <sub>2</sub>	Tholeiitic basalt 49.2 wt.% SiO <sub>2</sub>	Tholeiitic 49.67 wt.% SiO <sub>2</sub>
References	Sigmarrsson et al. (2011) and personal observation	Gjerløw et al. (2015)	Olafottir et al. (2008) and Olafottir et al. (2011)	Sigmarrsson et al. (2013)	Mattisson and Höskuldsson (2011) and personal communication	Eiriksson et al. (1994) and Jakobsson et al. (1978)

analyzer circulates a fluid containing the suspended grains though a lens in front of a camera, which captures 30 frames/s. Images have a resolution of 0.858 μm/pixel, which translates to a resolution range of 16,600 to 4200 pixels/particle for the chosen grain size. The images are processed as binary images and analyzed automatically by the PIdsa software. Predefined grain rejection criteria such as size, shape, darkness, and focus can be used to ensure data quality. We used a darkness threshold of 0.8 for grain detection and a circularity rejection of 0.98 to reject air bubbles created in the fluid from the dataset. Up to 28 shape parameters are reported on each analyzed grain and sample photos with grain data are available as well as general sample average statistics. For more information on the general setup, we refer to the PIdsa website.

We used a setup that generated 25 parameters on 20,000 grains for each sample (see Table 1). Many particle images are out of focus because the photos are taken while the grains are flowing, and samples were run with 90% focus rejection in order to ensure high image quality. Individual grain data were exported for grains with an equivalent area circle diameter (see Table 1) larger than 63 μm. The area-based size cutoff is also used to ensure a minimum of 4000 pixels/particles, which is much larger than the minimum of 750 pixels/particle recommended by Liu et al. (2015a).

### Shape parameters

The shape parameters are grouped into five overall shape models: circular, rectangular, ellipsoid, convex polygonal shape, and fiber (see Table 1). A short overview of each is given here.

The circular model converts the irregular grain into an equi-axis model, which is intuitive to interpret and easy to compare with other grains in terms of size, for example. This may also be convenient for tephra fall models that assume all particles are spheres. Different circle models are constructed either using equal area or perimeter of the grain or as a shape-bounding circle. All models are rotation independent.

The rectangular model is a single model based on the bounding rectangle yielding a length, width, and aspect ratio. A smallest rectangle is fit to the particle regardless of rotation, and it is thus orientation independent.

An ellipsoid model is built to better take particle shape irregularity into account. Analogous to the circular model, the ellipse has an equal area and a bounding model. The challenge of the ellipsoid model is that many major and minor axes can be defined from a specific area. To guide the choice of axes, the software chooses the axes with the same aspect ratio as the bounding rectangle and the actual amount of new information is thus very limited. This model is rotation dependent.

The polygon model is based on the convex hull shape and measures polygon order (i.e., number of sides on the fitted polygon) and convexity based on convex hull area. This model is also rotation independent.

The irregular model provides the caliper measures of Feret length and width, which are the smallest and largest possible distance between two parallel lines, and are thus by this definition rotation invariant (as opposed to other definitions in the literature of maximum and minimum pixel distances).

The fiber model is mostly intended for industrial use and uses a simple algorithm to straighten out long thin curved particles to rectangles.

We only discuss dimensionless parameters such as aspect ratio, form factor, and circularity (Table 1) because we are interested in the parameter changes between irregular magmatic grains and regular blocky phreatomagmatic grains and not the size diversity. However, because each dimensionless parameter only captures a limited amount of shape change, it is useful to analyze and combine the shape parameters to obtain as much shape information as possible while keeping it graphically simple.

### Building a reference grain dataset and modeling shape parameters

Thumbnail images from the six samples were used to identify and define a reference grain dataset. Initial qualitative observations indicate that the grains could not be divided into strictly blocky or vesicular grains. Some grains were blocky with no visible vesicles, but other grains had overall blocky shapes with bubbles disrupting the outline to a greater or lesser extent. Thus, grains with greater numbers of bubbles, or fewer larger bubbles, grew progressively more irregular (also observed by Liu et al. 2015a). There was no clear cutoff at which the grains went from generally blocky to generally irregular. Grains were therefore divided into four different classes: blocky, blocky-vesicular, vesicular, and elongate, based on their projection outlines (see Table 3). Blocky grains have a clearly regular outline. Vesicular grains have a clearly irregular outline. Blocky-vesicular grains have an overall blocky shape with a more or less irregular outline. The elongated grain class has a clear elongated appearance.

We assigned 75 grains to each class and then used the standard deviation normalized reference grain dataset for principal component analysis to identify the most important variation parameters for separating different grain types. Variation diagrams for the eruption bulk samples were subsequently generated based on the principal component analysis results.

The principal component analysis was run with a six non-dimensional parameter setup. Twenty of the reported parameters were related to the grain size variation between 63 and 125  $\mu\text{m}$  (lengths, widths, and diameters, see Table 1) or redundant aspect ratio measures. They were therefore removed

from the initial 26-parameter setup before the principal component analysis. The six parameters used were circularity, form factor, rectangularity, polygonal order, convexity, and Feret aspect ratio (see Table 1).

## Results

### Principal component analysis and parameter selection

The principal component analysis (PCA) shows that 96% of the data variance could be expressed by four components (Table 4). The first component, particle elongation, captures 62.24% of the variance. As particles get more elongated, the area-to-perimeter ratio changes as does the length-to-width ratio. The area-to-perimeter ratio change is tracked by form factor and circularity, while the length-to-width ratio change is found in the changing aspect ratio. Therefore, form factor, circularity, and aspect ratio contribute most to the first component (Table 4). However, elongation is best expressed by the particle aspect ratio, as form factor and circularity are also very sensitive to roughness changes, for example. We used the Feret aspect ratio because it is directly measured on the particle and is rotation invariant as measured by the PIDsa. This parameter alone efficiently separates the elongated grains from the rest (Fig. 2a).

The second most prominent variation (17.45%) was the change from regular to irregular morphology—or blocky to vesicular morphology (Fig. 2a). Rectangularity stands out as the primary contributor to this second component (Table 4), and it is one of the parameters that measure the overall shape of the grain by comparing the area of the particle with the area of the smallest bounding rectangle. This fits with the observed component trend in Fig. 2a.

Convexity, commonly known as solidity (Cioni et al. 2014; Liu et al. 2015a), and polygonal order describe the remaining shape variation of the reference grain population as the third component (9.52%) and the fourth component (6.88%) (Fig. 2b, c). Both parameters are related to the convex-hull shape of the particles and express the complexity of the overall grain geometry. However, the convexity variation is caused by a group of elongated grain outliers with very low convexities. This grouping cannot be correlated with other parameters or visual specifics. We interpret it as an image analysis error with regard to this specific parameter. Furthermore, when taking components 3 and 4 into account, it becomes clear that they do not reflect a morphology change from blocky to vesicular grains and instead their variation is perpendicular to the blocky-vesicular trend as seen on Fig. 2b, c.

Other parameters contribute essential information about irregularity shown by the trend from blocky to vesicular grains. Both circularity and form factor make important contributions as mentioned in the discussion of component 1.

**Table 3** Grain type morphology overview

	Blocky		Blocky-vesicular		Vesicular		Elongated	
<b>Pidsa images of representative grains</b>								
Regularity parameter	0.29	0.29	0.21	0.18	0.15	0.06	0.02	0.05
Feret aspect ratio	1.33	1.93	1.53	1.87	1.65	1.88	6.88	4.31
Convexity	0.92	0.91	0.88	0.90	0.84	0.84	0.97	0.89
Mean radius diameter	113 μm	106 μm	112 μm	111 μm	109 μm	99 μm	75 μm	105 μm
<b>SEM images of same grain type at comparable size</b>								
<b>Characteristics</b>	Straight perpendicular faces, rectangular outline		Straight perpendicular faces with few concavities, overall rectangular outline		Curved faces, irregular outline		Long thin grains, rectangular outline	
<b>Grain type group data</b>								
Regularity parameter (RP)	> 0.2		0.09-0.33		< 0.2		< 0.14	
RP arithmetic mean	0.30		0.20		0.12		0.05	
Feret aspect ratio (FAR)	< 2.6		< 2.6		< 2.6		> 2.6	
FAR arithmetic mean	1.59		1.82		1.94		4.98	
Convexity (CV)	> 0.85		> 0.83		> 0.79		> 0.81	
CV arithmetic mean	0.91		0.89		0.86		0.91	

Pidsa and SEM images are shown of a typical grain from each grain type, and the descriptive characteristics are given. For the Pidsa grains, the regularity parameter, Feret aspect ratio, and convexity measures are given for the shown grains. The mean radius diameter is given for size comparison. Finally, an overview of the parameters for the reference grain type groups is given stating the range of the given parameters as well as the arithmetic average for the grain type

Figure 2 shows that both form factor and circularity follow the blocky to vesicular grain trend in all diagrams. Circularity, like rectangularity, evaluates the overall morphology by comparing the area of the particle with the area of the bounding circle. The more regular, compact and equant a particle is, the closer both circularity and rectangularity are to 1. The form factor takes the smaller irregularities of the outline into account by comparing the particle's perimeter with the perimeter of a circle with the same area as the particle. Notice that elongated particles will have a very low form factor in spite of their smooth, regular outline. This is because by definition they are not equant. Following the examples of others (e.g., Dellino and La Volpe 1996), we combined the three parameters into a single factor to contain all the information in a

simple 2D diagram. We call it the regularity parameter, because it accounts for both the outline and overall shape aspects of regularity variation. It is defined as:

$$\text{Regularity parameter} = \text{Circularity} \times \text{Rectangularity} \times \text{Form factor.} \tag{1}$$

$$\text{Circularity} = \frac{4A_{\text{particle}}}{\pi d_{\text{BC}}^2} \tag{2}$$

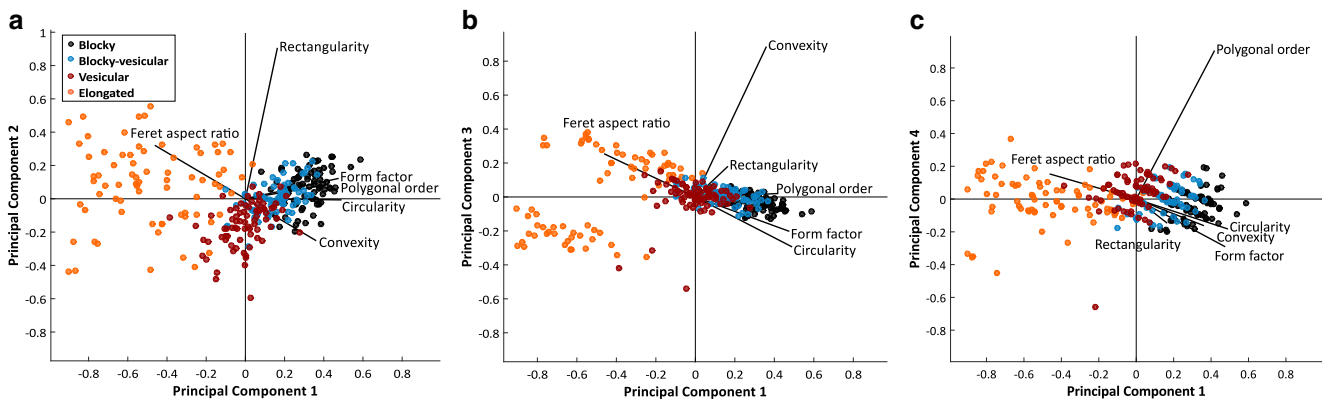
$$\text{Rectangularity} = \frac{A_{\text{particle}}}{l_{\text{BR}} w_{\text{BR}}} \tag{3}$$

$$\text{Form factor} = \frac{4\pi A_{\text{particle}}}{P_{\text{particle}}^2} \tag{4}$$

**Table 4** Principal component coefficients for all variables and percent of variance for each principal component

	Comp 1	Comp 2	Comp 3	Comp 4	Comp 5	Comp 6
Circularity	0.487	-0.0066	-0.2922	-0.1814	-0.0146	0.8027
Form Factor	0.4726	0.1214	-0.2011	-0.2891	0.6843	-0.4118
Rectangularity	0.1627	0.9023	0.1778	-0.1445	-0.3204	-0.065
Polygonal order	0.4168	0.0837	0.0201	0.902	0.0601	-0.04
Convexity	0.3583	-0.2496	0.8822	-0.161	0.0277	0.0659
Aspect ratio	-0.4592	0.3189	0.2527	0.1522	0.6515	0.4195
Percent of variance	62.2421	17.4474	9.5186	6.8809	2.3823	1.5287

Ninety-six percent of the reference grain variation is described by components 1 to 4



**Fig. 2** Principal component analysis for six variables on the reference grain dataset. **a** Principal component 2 vs. 1. **b** Principal component 3 vs. 1. **c** Principal component 4 vs. 1. See text and Table 4 for additional comments

Regularity parameter

$$= \frac{4A_{\text{particle}}}{\pi d_{\text{BC}}^2} \frac{A_{\text{particle}}}{l_{\text{BR}} w_{\text{BR}}} \frac{4\pi A_{\text{particle}}}{P_{\text{particle}}^2} = \frac{16A_{\text{particle}}^3}{d_{\text{BC}}^2 l_{\text{BR}} w_{\text{BR}} P_{\text{particle}}^2} \quad (5)$$

where  $A_{\text{particle}}$  = area of the particle projection,  $P_{\text{particle}}$  = perimeter of the particle projection,  $d_{\text{BC}}$  = diameter of the circle bounding, but not intersecting the particle projection,  $l_{\text{BR}}$  = length of the rectangle bounding, but not intersecting the projection, and  $w_{\text{BR}}$  = width of the rectangle bounding, but not intersecting the projection. All components of the regularity parameter are ratios from 0 to 1 and thus the regularity parameter is also a ratio ranging between 0 and 1. Regular, equant particles with smooth edges score close to 1 whereas irregularly shaped particles score close to 0.

The change from regular to irregular tephra grains reflects a change from blocky to vesicular and then to elongated grains. The form factor is very sensitive to the jagged irregular outline of vesicular grains and the high perimeter to area ratio of elongated grains. All three parameters are sensitive to the overall morphology change from compact blocky equant grains to irregular vesicular and elongated grains. The regularity parameter is therefore good for distinguishing between blocky and vesicular particles (Table 3; Fig. 3a).

**Particle insight shape analyzer data reproducibility**

The PIdsa was not specifically designed to run tephra samples and the stability of the shape parameter output was tested by six runs of the same sample under the same conditions. Standard deviations on the means of the dimensionless parameters of circularity, rectangularity, form factor, convexity, and Feret aspect ratio range from 0.07% to 0.23% (Table 5). This translates into a standard deviation of 0.77% for the regularity parameter (Table 5). The same parameters were tested for normality with normal probability plots, and all show normal distributions for a minimum of 99% of the distribution (Electronic supplementary material Fig. 2). *t* tests were used to test for dissimilarity between adjacent sample runs as well as sample runs with the largest

difference in parameter mean value. *p* value recommendations of Johnson (2013) were followed, so *p* values <0.005 reject the null hypothesis (Table 5). Only 2 of the 36 *t* tests resulted in a rejection of the null hypothesis. Based on the low standard deviations and the *t* test results, the data are considered reproducible.

**Statistical verification of grain types**

*T* tests between all reference grain types were performed to test if the grain types are statistically significantly different (Table 6). All results of regularity parameter, form factor, and circularity reject the null hypothesis and are thus successful in distinguishing between shape types. Rectangularity for blocky-vesicular and vesicular grains is not statistically dissimilar. This is also true of the Feret aspect ratio *t* test of blocky-vesicular and elongated distributions. However, the overall result of the *t* tests show that the regularity parameter combined with the Feret aspect ratio is effective in separating the grain types.

**Statistical significance of different deposits**

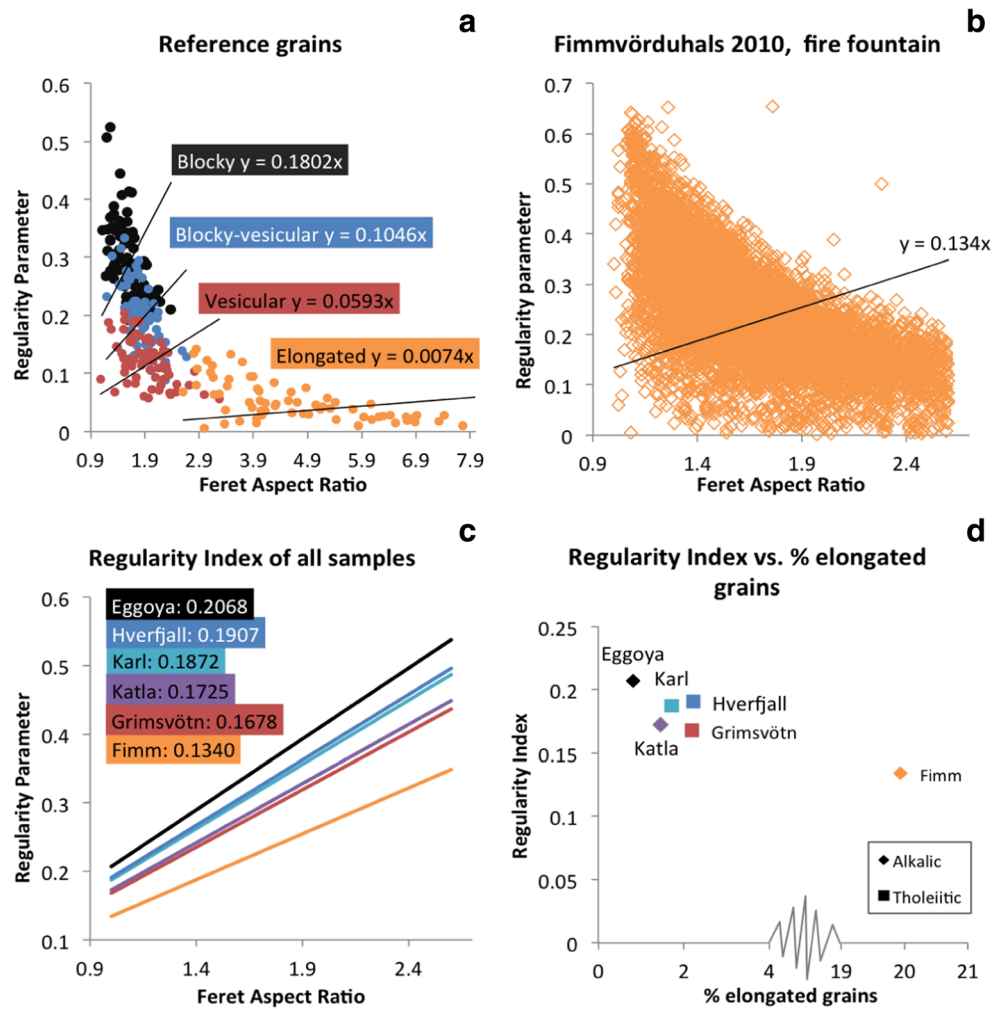
Finally, all the samples were compared with each other by *t* tests of the shape parameter circularity, rectangularity, form factor, Feret aspect ratio, and regularity parameter. Only 6 of the 75 *t* tests reject the null hypothesis, and the 6 eruption samples are considered significantly different in terms of their shape parameters.

**The regularity index**

Based on the results of the PCA, we constructed a classification diagram using the Feret aspect ratio and the regularity parameter (Fig. 3a). The plot quantitatively characterizes the ash from the different eruption environments. It is possible to separate blocky, vesicular, and elongated reference grains (Fig. 3a), although adjacent shape groups overlap due to transitional grains. These transitional grains become important when the whole sample grain morphologies are plotted



**Fig. 3** **a** All reference grains plotted with regularity against elongation. Graphical average lines through (0,0) show the difference between grain types as inclinations of the slope. **b** Showing grains from the Fimmvödurhals sample in a “regularity against elongation” plot. Elongated grains have been removed. A graphical average line with manipulated starting point is shown to illustrate the average regularity of the whole population. **c** All sample average lines plotted in a plot similar to (b) and showing the regularity index of each eruption deposit. **d** Correlating regularity index, percentage of elongated grains, and geochemistry. See text for additional comments



(Fig. 3b) and individual grain types cannot be distinguished. Cutoff values for grain types are given in Table 3 based on the 300 reference grains.

In order to focus the quantitative study on the active ash particles generated by the explosion, elongated grains generated by ductile fragmentation (Büttner et al. 2002) were

**Table 5** Reproducibility tested by running the same subsample consecutively six times

Reproducibility and dissimilarity	Circularity	Form factor	Rectangularity	Convexity	Feret aspect ratio	Regularity factor	Regularity index
Mean of sample means	0.642045427	0.68149016	0.703576096	0.893492635	1.466746758	0.289339024	0.19615 <sup>a</sup>
Standard deviation, all runs	0.000770942	0.001555488	0.000473191	0.000607576	0.002284821	0.002224955	0.000992891
Standard deviation	0.120%	0.228%	0.067%	0.068%	0.156%	0.769%	0.506%
<i>t</i> test 2–2, 2–3	0.598571526	0.000128061	0.859760127	0.268307558	0.541316593	0.027402511	
<i>t</i> test 2–3, 2–4	0.806764454	0.658252344	0.396769053	0.898315488	0.482365366	0.816127473	
<i>t</i> test 2–4, 2–5	0.636078303	0.791632872	0.548264641	0.24455235	0.974518866	0.816502623	
<i>t</i> test 2–5, 2–6	0.24897216	0.484885537	0.995892164	0.474223264	0.291492419	0.340340108	
<i>t</i> test 2–6, 2–7	0.045237502	0.122738053	0.044922286	0.679838823	0.026149296	0.043885719	
<i>t</i> test between samples with largest difference in mean	0.045237502 (2–6, 2–7)	7.58856E-05 (2–2, 2–7)	0.046570228 (2–5, 2–7)	0.150868397 (2–4, 2–7)	0.026149296 (2–6, 2–7)	0.199501127 (2–2, 2–6)	

The low standard deviations all below 1% show a good precision of the method. *t* tests were also performed on consecutive runs and on runs with the largest difference in the mean of the parameter. Only two tests show dissimilarity of a single parameter (<0.005) (Johnson 2013)

<sup>a</sup> Mean of the regularity index of all runs

**Table 6** T tests of the dissimilarity between the shape parameters of the different grain types

Reference grain types	Circularity	Form factor	Rectangularity	Feret aspect ratio	Regularity factor
Blocky vs. blocky-vesicular	7.28633E-13	1.79975E-21	0.001206307	3.23483E-07	1.97618E-20
Blocky vs. vesicular	4.40146E-28	1.77909E-48	4.11322E-22	3.81556E-09	4.72646E-05
Blocky vs. elongated	4.37849E-70	4.61729E-57	0.001312259	8.01789E-29	6.14298E-59
Blocky-vesicular vs. vesicular	8.65214E-10	5.1706E-13	1.37356E-15	0.035989286	4.24739E-18
Blocky-vesicular vs. elongated	2.19939E-59	2.95902E-36	0.137023985	5.23038E-27	6.97522E-43
Vesicular vs. elongated	4.62724E-42	5.1776E-20	0.000120391	2.71972E-26	3.73693E-25

All but two parameters are shown to be dissimilar by the  $p < 0.005$  criterion (Johnson 2013). Only the Feret aspect ratio of the blocky-vesicular vs. vesicular distributions and the rectangularity of blocky-vesicular vs. elongated distributions do not reject the null hypothesis. This shows that the grain types display well-defined distributions compared with one another

removed by the cutoff values in Table 3. An important observation is that all eruption deposits contain the whole spectrum of grain types within the measured grain size interval (see Electronic supplementary material Fig. 3). Therefore, the sheer amount of data points in each plot (around 15,000–17,000 points) makes any visual distinction impossible. To quantify the difference, we have projected the points onto a line through (0,0) using a linear regression. The line serves as a graphical average of the distribution, and the slope is a measure of the average regularity of the grains. The (0,0) constraint has been invoked so all the lines have the same starting point and the slope of the lines are directly comparable. We also prefer to have a positive slope, so it follows the same logic as the shape change. The higher the regularity parameter of a grain the higher it plots in the diagram. Thus, the more regular and blocky a grain population is, the steeper the slope is and the higher the slope value is. Conversely, a population with very jagged, elongated, and irregular grains will have a much flatter regression line and a lower slope value. We have termed the slope value the regularity index (RI) and we note the slope is strictly a modeling tool that is used to quantify the relative amounts of blocky vs. vesicular and elongated grains.

Values of the RI of the six samples are given in Fig. 3c. The sample with the most irregular grains is the Fimmvörduháls fire fountain sample, which has the lowest RI of  $0.134 \pm 0.001$  ( $2\sigma$ ). Then follows the subglacial tephra samples from the Grimsvötn and the Katla eruptions, which have intermediate RIs of  $0.168 \pm 0.002$  ( $2\sigma$ ) and  $0.173 \pm 0.002$  ( $2\sigma$ ), respectively. The highest RI ( $0.207 \pm 0.002$  ( $2\sigma$ )) is exhibited by the sample of the Surtseyan eruption in Eggöya, Jan Mayen, whereas the sample from other Surtseyan eruption of Karl shows a slightly lower RI of  $0.187 \pm 0.002$  ( $2\sigma$ ). The latter is comparable with the tephra from the wet fissure eruption sample from Hverfjall, which has a RI of  $0.191 \pm 0.002$  ( $2\sigma$ ). There is no apparent correlation between the fraction of elongated grains and the RI (Fig. 3d). However, there is a tentative correlation between geochemistry and RI for some eruption environments. In the submarine environment the alkalic Eggöya sample has a higher index than the tholeiitic Karl

sample. Between the subglacial samples the trans-alkalic Katla sample has a slightly higher index than the tholeiitic Grimsvötn sample.

## Discussion

### Points of awareness using the PIdsa method

The sheer rapidity (20,000 grains in about 30–45 min) makes this method attractive and useable. The equipment is small, easy to run, and requires only simple sample preparation. Its main advantage is that it characterizes many grains from random angles, which allows for more accurate and complex grain shape models. However, it is clear upon examining results and thumbnail images that the use of a moving medium involves some challenges. Firstly, each sample should run for a limited time only. Small grains may start to wash out from the larger grains and thereby change the optical properties of the fluid slightly. Using wet sieving methods or prewashing the dry-sieved samples can resolve the issue to some extent, so samples can run for longer if needed.

Another challenge is defining the dark threshold and the camera gain. There is a balance between detecting clear grains and getting a well-defined dark-grain outline. This will mostly be a challenge for samples with transparent tephra grains such as silicic ash. Finally, high focus rejection is important to ensure data quality (90% is recommended). High focus rejection, however, limits the analyzed grain size to the larger part of the dispersed grains. Reruns on the same  $<125 \mu\text{m}$  grain size sample with 90% focus rejection and then 30% focus rejection show a shift in average mean radius diameter from 81.6 to 46.1  $\mu\text{m}$ .

### Resolution and the perimeter value issue revisited

The resolution of the OPA imagery determines the baseline data quality. Outline irregularity is one of the key features that distinguish magmatic tephra from phreatomagmatic tephra,

and the perimeter is the central parameter in gaining this information. Therefore most studies use parameters highly sensitive to perimeter changes (e.g., Dellino and La Volpe 1996; Büttner et al. 2002; Jordan et al. 2014; Leibrandt and Le Pennec 2015; Liu et al. 2015a), but as previously discussed, perimeter measurements are resolution dependent. This becomes an issue when dealing with a stationary imaging setup for a range of grain sizes. While some studies have overcome this obstacle by manually normalizing the OPA imagery to a specific resolution (e.g., Liu et al. 2015a; Dürig et al. 2012), this option defies the objective of automated bulk analysis. As the imaging setup is usually stationary and the pixel/area is constant for all images, the resolution effectively drops significantly for smaller grains, thus decreasing the perimeter value. This means that smaller grains will seem smoother compared with larger grains of similar shape. This effect is evident in the dataset by Leibrandt and Le Pennec (2015). They provide average convexity (see Table 1 for definition) data of 1500 particles in  $0.5 \varphi$  sieving intervals. They show grain sizes ranging from  $0.5$  to  $5.5 \varphi$  ( $0.710$  to  $0.023$  mm) from one bulk sample at a fixed magnification. Including data using different magnifications makes it possible to evaluate whether the parameter change is a real shape change or an artifact of the resolution. When comparing the constant magnification data with higher magnifications, it is evident that the change is indeed an artifact of perimeter resolution (Leibrandt and Le Pennec 2015). Based on the published diagram of the Leibrandt and Le Pennec (2015) dataset, we have found a quantitative change in bulk average of the convexity parameter of less than 2% in the  $3$  to  $4 \varphi$  size range. Liu et al. (2015a) find that changing the resolution from  $10^6$  to  $10^2$  pixels/particle increases convexity of a single grain by a factor of 2–3 depending on the grain morphology. However, that would correspond to a size range from, e.g.,  $3$  to  $10 \varphi$  ( $0.125$  to  $0.00125$  mm) or about  $-2.5$  to  $4 \varphi$  ( $6.3$  to  $0.063$  mm), which are orders of magnitude from the grain size range of current-automated morphology studies. Thus, the resolution difference in the limited size range of  $3$  to  $4 \varphi$  should not pose problems for the data quality.

Additionally, perimeter parameter values from different studies with different image resolution/grain sizes cannot be compared. Unfortunately, most of the IPA studies reported in the literature are focused on perimeter parameters and thus comparing results between different studies remains difficult.

### Applicability of established classification diagrams to PIdsa data and automated bulk analysis

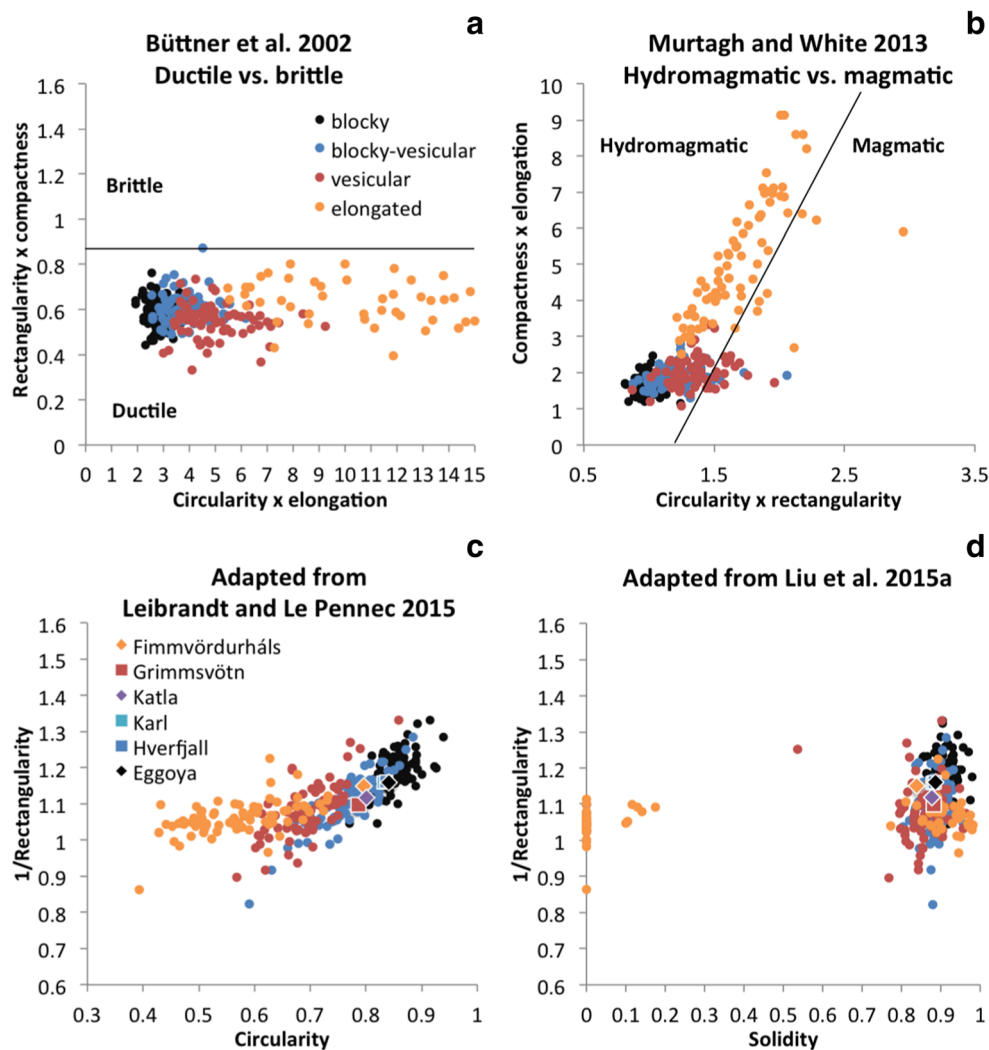
When comparing the different classification diagrams of Büttner et al. (2002), Murtagh and White (2013), and Liu et al. (2015a), it is apparent that these authors have shown no quantitative way to deal with bulk samples containing a broad mix of all morphologies and only quantify shape

changes of single grains. Liu et al. (2015a, b) presents a bulk analysis of tephra from Grimsvötn 2011, which plots all across the classification diagram—as observed in our study. Leibrandt and Le Pennec (2015) treat bulk datasets and deal with bulk averages in their classification diagram, but a lot of morphology distribution information is lost in this way. Many different morphology distributions may result in the same average value, although the generic implications may be vastly different. Therefore, we encourage the use of what we term a graphical average model instead, so that the overall point distribution may be visually inspected.

For comparison, we plotted our reference grains and samples onto the classification diagrams of Büttner et al. (2002), Murtagh and White (2013), Leibrandt and Le Pennec (2015), and Liu et al. (2015a) (Fig. 4). For the Büttner et al. (2002) and Murtagh and White (2013) diagrams, we had to recalculate our data to reflect circularity, rectangularity, and compactness as defined in these diagrams (Table 1, Dellino and LaVolpe 1996). Unfortunately, elongation cannot be obtained from our dataset in the exact same way, so instead we have used the Feret length as the long axis and calculated a perpendicular mean based on the particle area (Table 1). For the Leibrandt and Le Pennec (2015) and Liu et al. (2015a) diagrams, we have used circularity and solidity as defined. Both diagrams use convexity, which cannot be obtained from our dataset and thus leaves these diagrams ill-suited for the interpretation of the PIdsa dataset. However, in an attempt to revise the diagrams to accommodate the PIdsa data, we have followed the recommendations of Liu et al. (2015a) and chosen a shape parameter from the same cluster analysis parameter group as convexity. In three out of four cluster analyses, rectangularity (of Dellino and LaVolpe 1996) follows convexity in the same position in the diagram (Liu et al. 2015a) and is therefore chosen as the best replacement parameter. The major difference between the two parameters is that rectangularity is not bound between 1 and 0 because the bounding rectangle does not define the shortest perimeter of the grain. Additionally, to follow the same graphical logic as the original diagrams, we have inverted the Dellino and LaVolpe (1996) rectangularity ( $1/\text{rectangularity}$ ), but it should be kept in mind that the grain distribution does not approach (1,1).

The four comparative plots are shown in Fig. 4. In the Büttner et al. (2002) diagram (Fig. 4a), all reference grains are classified as ductile, while the Murtagh and White (2013) diagram (Fig. 4b) classifies almost all reference grains as hydromagmatic. None of these obscure classifications can be explained by our slight adaptation of the elongation equation, and so these two diagrams do not represent our dataset well. Nemeth and Cronin (2011) used light microscopy, scanning electron microscopy, and backscatter electron microscopy to obtain images of tephra grains, which were subsequently turned into binary images and analyzed by the ImageJ software package. Their study shows that the data

**Fig. 4** PIdsa data plotted in the most commonly used classification diagrams related to tephra grain morphology. **a** Diagram first presented by Dellino and LaVolpe (1996) and Buttner et al. (2002) subsequently added the ductile/brittle fields based on MFCI experiments. The parameters used in this diagram can be recalculated from PIdsa data except for elongation. We have defined a substitute elongation. All parameter calculations are shown in Table 1 (Dellino and LaVolpe 1996). **b** Diagram from Murtagh and White (2013). Parameters are the same as used by Dellino and La Volpe (1996), but they are combined in a different way on the two axes. **c** Adapted from Leibrandt and Le Penneec (2015). Parameter definitions are shown in Table 1 (Leibrandt and Le Penneec 2015). As the convexity parameter of Leibrandt and Le Penneec (2015) could not be obtained from the PIdsa, we have used rectangularity as defined by Dellino and La Volpe (1996) (Table 1). See text for additional comments. **d** Diagram adapted from Liu et al. (2015a). Parameter definitions are shown in Table 1. Again, convexity has been replaced by rectangularity. See text for further comments



distribution is controlled by the imaging method. Both light microscopy and scanning electron microscopy data plot in the ductile field of Büttner et al. (2002), while all backscatter electron data falls in the brittle field for the same samples. Thus, the distribution of our reference grains might be controlled by the imaging method. Either way the diagrams are not appropriate for interpretation of our PIdsa data.

In the diagram adapted from Leibrandt and Le Penneec (2015) (Fig. 4c), the reference particles are spread out and blocky and vesicular particles rarely overlap. However, when applying the method of averages to our samples, the distinction between different bulk samples from different eruption sites is not well defined. The six bulk samples fall in two groups consisting of (1) Fimmvödurhals, Grimsvötn, and Katla and (2) Karl, Hverfjall, and Eggoya. Thus, the overall division is the same as shown in Fig. 3 by using the RI, but the averages do not provide a quantitative comparable measure and this makes it hard to interpret the differences between bulk samples. So, although it is useful to differentiate between our reference grains, it is less effective for bulk samples of similar chemical composition using the proposed method of bulk averages.

In the diagram adopted from Liu et al. (2015a) (Fig. 4d), the instability issue of our solidity parameter for elongated grains is evident. The rest of the reference grains plot with the blocky grains in the upper left part and vesicular and elongated grains plot in the lower part. But the groups overlap significantly and are not as well-defined and systematic as reflected in the Leibrandt and Le Penneec (2015) plot. The same can be said for the eruption bulk sample averages. Thus, the adapted version of the Liu et al. (2015a) diagram is not helpful in interpreting our dataset.

Our overall conclusion is that the existing diagrams and discrimination methods are not adequate to characterize our dataset. This may be due to different imaging setups, where our setup is the only dynamic one, or it could be related to different image processing conditions and differences in grain sizes. However, it may also be explained as an artifact of diagrams created on the basis of very different reference grains. The Büttner et al. (2002) diagram was based on experimental grains of MFCI without any vesiculation taking place. All our samples show evidence of some vesiculation and they might not be appropriate for the Büttner et al. (2002) plot.

The magmatic/hydromagmatic fields in the Murtagh and White (2013) diagram were drawn from an equation from a study comparing end-member products of Kilauea Iki ash and Loi'hi seamount ash. Thus, the reference grains are very similar to this study as they are basaltic and include similar environments with similar grain types (except for quench granulation grains from seamounts). But the means of deriving the equation is not published and the classification differences remain unresolved.

The Leibrandt and Le Pennec (2015) diagram was constructed from andesitic reference samples with comparable geochemical compositions but different eruption styles (Strombolian and subplinian, Leibrandt and Le Pennec 2015). Thus, the sample setup resembles our study and might explain why this diagram is the most useful for our dataset as depicted by the plotted systematics of our reference grains (Fig. 4c).

The diagram of Liu et al. (2015a) builds on convex hull shape parameters. We have previously shown that our analysis provides ambiguous solidity results particularly for elongated grains. Therefore, this diagram cannot be used to accurately evaluate our dataset. Furthermore, the diagram was made to illustrate different grain types and is therefore based on reference samples from vastly different eruption styles. Samples also range from mafic to silicic compositions. Blocky reference particles are taken from submarine quench granulation of basalt, while the vesicular grains are from basaltic to dacitic eruptions. There is no ambiguity in telling these particles apart even without shape parameters, so it is not surprising that shape parameters do a good job of separating them. Our reference grains were picked out from a much narrower variation interval as all samples share approximately the same geochemistry and crystal content. This could also limit the applicability of the Liu et al. (2015a) diagram to our dataset.

In summary, we suggest the use of a diagram for the PIdsa dataset based mostly on area- and dimension-ratio parameters in which grain shape changes continuously and where the whole bulk dataset is shown.

### Volcanological implications of the grain-type distribution

The presence of all grain types in all eruption deposits suggest that brittle fragmentation is more complex than traditionally reflected in classification diagrams. This is probably related to the studied grain size, which supports the detection of both blocky and vesicular (irregular) grains. Liu et al. (2015b) recognized that the grain size and morphology of tephra from the Grimsvötn 2011 eruption was related to prefragmentation bubble size and distribution. They showed that the proportion of dense fragments (without vesicles) grew to up to 80% as the grain size approached that of the modal vesicle diameter (15–25  $\mu\text{m}$ ). At 63–91  $\mu\text{m}$ , 60% of the grains were dense and the

rest vesicular, whereas about only 25–10% of the grains were dense in the 91–125-grain-size fraction. Thus, the choice of studied grain size is critical to volcanological interpretations. An example of this is the work of Honnorez and Kirst (1975): their results are most probably an artifact of comparing particles from grain sizes 2 orders of magnitude apart. The particles in their quench fields (Fig. 4) are primarily in the range of 0.08 to 0.05 mm, whereas the grains in their explosive granulation fields (Fig. 4), all range from a few millimeters up to centimeters in size. The fields are set apart by the number of corners or inflection points in the grain perimeter and the planarity fields (percentage of plain grain perimeter). Thus, the distribution of samples is readily explained as pertaining to larger vesicle-populations being preserved in the larger grains—or the change from a simple particle-dominated sample to a complex particle-dominated sample (Genareau et al. 2013).

However, the grain-type diversity in all deposits needs an explanation and therefore the fragmentation dynamics must be considered. The eruption style of fire fountaining has been attributed to volatile-coupled ascent of basaltic magma, with mono-modal or bimodal vesicle size distributions found in fire fountain clasts (e.g., Parfitt and Wilson 1995; Mangan and Cashman 1996; Stovall et al. 2011; Jutzeler et al. 2016). Pre-fragmentation heterogeneity in vesicle size for fire fountains has been observed (Stovall et al. 2011) spanning as much as 3 orders of magnitude, which can thus produce different sizes of simple ash grains (Genareau et al. 2013). Large dense simple ash grains would settle out close to the fountains, which is where the sampling of Fimmvörduhals was done. These simple ash grains could, in some orientations, be characterized as blocky or blocky-vesicular grains by the PIdsa analysis.

Another possible process might relate to post-fragmentation alteration. Post-fragmentation vesicle size heterogeneity is very commonly observed in fire fountain clasts (e.g., Mangan and Cashman 1996; Schipper et al. 2010; Stovall et al. 2011). However, the post-fragmentation bubble expansion and coalescence process usually produces thin bubble walls and small plateaus (Mangan and Cashman 1996; Parfitt and Wilson 1995; Jutzeler et al. 2016) and it is likely not the cause of the blocky grains observed in the analyzed size range. Other explanations could be brittle fragmentation of degassed recycled clasts, but this is mostly a concern in pulsatory eruptions such as Strombolian or Surtseyan and probably not a valid explanation in fire fountains (d'Oriano et al. 2014). We suggest that the presence of blocky and blocky-vesicular grains in the fire fountain deposit is related to the prefragmentation vesicle size distribution.

Genareau et al. (2013) found that complex ash particles (bubbly ash grains preserving more than one vesicle indentation) preserve prefragmentation vesicle sizes with no post-fragmentation expansion features complicating the analysis. They also showed a method for determining the vesicle size distribution for complex ash-sized particles in the 50–125  $\mu\text{m}$

size range. It would be interesting to compare the results from vesicle size studies like Genareau et al. (2013) with a PIdsa dataset for the same samples.

The presence of irregular vesicular grains in the phreatomagmatic eruptive settings can be explained by prefragmentation vesiculation (Liu et al. 2015b). Other recent studies have reported on the prefragmentation vesicle size and volume distributions in subaqueous environments, such as submarine (e.g., Schipper et al. 2010, 2011a; Jutzeler et al. 2016), glacial lake (Graettinger et al. 2013), and Surtseyan eruptions (e.g., Murtagh and White 2013; Schipper and White 2016). They conclude that the eruption style is related to the prefragmentation volatile-coupled or de-coupled ascent of the magma. Thus the prefragmentation vesiculation processes play a vital role in the phreatomagmatic eruptions and can explain the presence of vesicular grains.

### Volcanological implications of the regularity index results

Our classification scheme allows for quantitative comparison of the morphology of populations of ash grains generated in different eruptive settings. The general systematics of the RI conforms to the established shape interpretation scheme by showing that wet eruptions have blockier and more equant particles than dry eruptions. The advantage of using a grain population-based index is that the rigid binary classification of magmatic/phreatomagmatic can be transformed into a fragmentation spectrum. The spectrum end-members represent the phreatomagmatic fragmentation (high RI) and the dry magmatic fragmentation (low RI). Intermediate RI values represent mixed fragmentation processes. Interestingly, the intermediate RI values in this study are related to eruptions of subglacial central volcanoes, where magmatic degassing have been shown to play a significant role in the fragmentation process for silicic melts (Owen et al. 2013) as well as for the Grimsvötn 2011 eruption (Liu et al. 2015b). Data from Hreinsdottir et al. (2014) shows that the height of the Grimsvötn 2011 eruption column correlated with the rate of pressure change in the underlying magma chamber. This observation supports the influence of prefragmentation volatile exsolution on the eruption style. Liu et al. (2015b) suggest that thermal stresses play a role in the fragmentation process and argue that their data supports an initial fluidal (ductile) magmatic fragmentation followed by brittle thermal granulation of thermally stressed vesicular particles. Graettinger et al. (2013) also report a tephra sequence from a subaqueous glacier lake eruption at Askja volcano, Iceland, with fluidal textures. However, their deposit sequence changes from fluidal-dominated textures to a fine blocky ash deposit indicating that the more effective brittle fragmentation mechanism of MFCI takes over. Considering the plume heights of the Grimsvötn 2011 eruption of 20 km, we consider the brittle thermal

granulation to be a secondary fragmentation mechanism to MFCI in this eruption as well.

Schipper and White (2016) looked at fragmentation in Surtseyan eruptions and found that it is the mingling of magma and water in MFCIs that drives them. Graettinger et al. (2013) suggests that the magmatic ductile fragmentation can enable the fuel-coolant premix that leads to MFCI explosions. Conversely, the shockwave from MFCI explosions can cause rapid depressurization of the magma and trigger magmatic explosions. This feedback mechanism could explain the varying content of vesicular grains between our two Surtseyan deposit samples and relate it to differences in the volatile exsolution history of each eruption.

The findings from Hreinsdottir et al. (2014) and Schipper and White (2016) can also explain a part of our quantitative dataset. They suggest that the higher the RI gets the more the MFCI has controlled the fragmentation process. This is supported by the data from Liu et al. (2015b), where our intermediate RI for Grimsvötn 2011 deposit correlates with 60–25% blocky grains in our analyzed size range.

The above fragmentation interpretation of our RI is based on the assumption that the irregular grains are related to magmatic degassing and vesiculation, whereas blocky grains are related to phreatomagmatic explosions. Such an interpretation should be used carefully, as grain shapes are highly influenced by phenocryst and microlite content (Schipper et al. 2010; Jutzeler et al. 2016). Therefore, our fragmentation spectrum can only be directly applied to phenocryst- and microlite-poor tephra of basaltic composition at present.

### Conclusion

Our analysis of grain populations shows that both Surtseyan, subglacial and fire fountain eruptions produce a similar range of shapes from blocky to vesicular as well as elongated grains. We suggest that the analyzed particle morphologies are directly related to the fragmentation mechanisms. We have tested our dataset in four different published classification diagrams for tephra grains. This test shows that while other diagrams are successful at classifying the grain shape they are not useful for interpreting our bulk datasets and they do not provide a means for quantitatively comparing bulk samples.

To deal with the lack of comparability among existing classifications, we have defined a regularity parameter and demonstrate how the regularity of grain shape can be used to distinguish between blocky and vesicular grains. Then, we designed a diagram plotting regularity against elongation, which shows a systematic change from blocky grains to vesicular grains and which allows for graphic averaging of the shape of an entire grain population. This average is a measure of the overall grain regularity and can be used as an index of regularity of the population. Our results show that the RI

differs for different eruptive settings. Submarine and lacustrine eruptions produce the most regular grains with regularity indices of 0.207–0.187. A fissure eruption produces mostly irregular grains with an index of 0.134, whereas subglacial eruptions produce intermediate averages with indices of 0.168–0.173. If the RI is used as a fragmentation proxy, then our initial results suggest that both phreatomagmatic explosions as well as magmatic degassing play a significant role in the active subglacial eruption fragmentation.

The systematic change in indices between wet and dry eruptions suggests that the RI can be used to assess the role of magmatic vs. phreatomagmatic fragmentation. This could be very helpful in active eruption scenarios and hazard studies. Other interesting perspectives could arise from looking at changes in RI with increased microlite content, increased silica content, or systematically varying volatile content.

Future work should consider combining PIdsa analysis with thorough vesicle size distribution studies on the same samples and adding samples from Strombolian and Plinian eruptions.

**Acknowledgements** Our sincere gratitude goes to Eirik Gjerløw and Jónas Guðnason for providing samples from Jan Mayen and Grímsvötn. Our grateful thanks are also extended to Guðrún Larsen for advice and assistance with fieldwork and to Tobias Dürig, Bergrun Óladóttir, Tinna Jónsdóttir, Agnes Magnúsdóttir, Emma Liu, and Kathy Cashman for the many interesting discussions. Finally, we warmly acknowledge the helpful comments and suggestions of P. Dellino, K. Cashman, and three anonymous reviewers.

## References

- Bagheri GH, Bonadonna C, Manzella I, Vonlanthen P (2015) On the characterization of size and shape of irregular particles. *Powder Technol* 270:141–153
- Buttner R, Dellino P, La Volpe L, Lorenz V, Zimanowski B (2002) Thermohydraulic explosions in phreatomagmatic eruptions as evidenced by the comparison between pyroclasts and products from molten fuel coolant interaction experiments. *J Geophys Res* 107(B11):2277. doi:10.1029/2001JB000511
- Cioni R, D'Oriano C, Bertagnini A (2008) Fingerprinting ash deposits of small scale eruptions by their physical and textural features. *J Volcanol Geotherm Res* 177(1):277–287
- Cioni R, Pistolesi M, Bertagnini A, Bonadonna C, Hoskuldsson A, Scateni B (2014) Insights into the dynamics and evolution of the 2010 Eyjafjallajökull summit eruption (Iceland) provided by volcanic ash textures. *Earth Planet Sci Lett* 394:111–123
- Coltelli M, Miraglia L, Scollo S (2008) Characterization of shape and terminal velocity of tephra particles erupted during the 2002 eruption of Etna volcano, Italy. *Bull Volcanol* 70(9):1103–1112
- Dellino P, LaVolpe L (1996) Image processing analysis in reconstructing fragmentation and transportation mechanisms of pyroclastic deposits. The case of Monte Pilato-Rocche Rosse eruptions, Lipari (Aeolian islands, Italy). *J Volcanol Geotherm Res* 71(1):13–29
- Dellino P, Liotino G (2002) The fractal and multifractal dimension of volcanic ash particles contour: a test study on the utility and volcanological relevance. *J Volcanol Geotherm Res* 113(1–2):1–18
- Dellino P, Mele D, Bonasia R, Braia G, La Volpe L, Sulpizio R (2005) The analysis of the influence of pumice shape on its terminal velocity. *Geophys Res Lett* 32(21):L21306. doi:10.1029/2005GL023954
- Dellino P, Gudmundsson MT, Larsen G, Mele D, Stevenson JA, Thordarson T, Zimanowski B (2012) Ash from the Eyjafjallajökull eruption (Iceland): fragmentation processes and aerodynamic behavior. *J Geophys Res-Sol Ea* 117:B00C04. doi:10.1029/2011JB008726
- D'Oriano C, Bertagnini A, Cioni R, Pompilio M (2014) Identifying recycled ash in basaltic eruptions. *Scientific Reports* 4:5851. doi:10.1038/srep05851
- Dürig T, Mele D, Dellino P, Zimanowski B (2012) Comparative analyses of glass fragments from brittle fracture experiments and volcanic ash particles. *Bull Volcanol* 74(3):691–704
- Eiriksson JS, Sigurgeirsson MA, Hoelstad T (1994) Image analysis and morphometry of hydromagmatic and magmatic tephra grains, Reykjanes volcanic system, Iceland. *Jökull* 44:41–55
- Ersøy O, Gourgaud A, Aydar E, Chinga G, Thouret J-C (2007) Quantitative scanning-electron microscope analysis of volcanic ash surfaces: application to the 1982–1983 Galunggung eruption (Indonesia). *Geol Soc Am Bull* 119(5–6):743–752
- Genareau K, Mulukutla GK, Proussevitch AA, Durant AJ, Rose WI, Sahagian DL (2013) The size range of bubbles that produce ash during explosive volcanic eruptions. *J Appl Volcanol* 2(1):1–18
- Gjerløw E, Höskuldsson A, Pedersen R-B (2015) The 1732 Surtseyan eruption of Eggöya, Jan Mayen, North Atlantic: deposits, distribution, chemistry and chronology. *Bull Volcanol* 77(2):14. doi:10.1007/s00445-014-0895-6
- Graettinger AH, Skilling I, McGarvie D, Hoskuldsson A (2013) Subaqueous basaltic magmatic explosions trigger phreatomagmatism: a case study from Askja, Iceland. *J Volcanol Geotherm Res* 264:17–35
- Heiken G (1972) Morphology and petrography of volcanic ashes. *Geol Soc Am Bull* 83(7):1961–1988
- Heiken G (1974) An Atlas of volcanic ash. Smithsonian. *Contrib Earth Sci* 12:1–101
- Honnorez JK, Kirst P (1975) Submarine basaltic volcanism: morphometric parameters for discriminating hyaloclastites from hyalotuffs. *Bull Volcanol* 39:441–465
- Hreinsdóttir S, Sigmundsson F, Roberts MJ, Björnsson H, Grapenthin R, Arason P, Arnadóttir T, Holmjarn J, Geirsson H, Bennett RA, Gudmundsson MT, Oddsson B, Ofeigsson BG, Villemín T, Jonsson T, Sturkell E, Hoskuldsson A, Larsen G, Thordarson T, Óladóttir BA (2014) Volcanic plume height correlated with magma-pressure change at Grímsvötn Volcano, Iceland. *Nat Geosci* 7(3):214–218
- Jakobsson SP, Jonsson J, Shido F (1978) Petrology of the Western Reykjanes Peninsula, Iceland. *J Petrol* 19(4):669–705
- Johnson VE (2013) Revised standards for statistical evidence. *Proc Natl Acad Sci U S A* 110(48):19313–19317
- Jordan SC, Dürig T, Cas RAF, Zimanowski B (2014) Processes controlling the shape of ash particles: results of statistical IPA. *J Volcanol Geotherm Res* 288:19–27
- Jutzeler M, White JDL, Proussevitch AA, Gordeev SM (2016) Vesiculation and fragmentation history in a submarine scoria cone-forming eruption, an example from Nishiizu (Izu Peninsula, Japan). *Bull Volcanol* 78(2)
- Leibrandt S, Le Pennec JL (2015) Towards fast and routine analysis of volcanic ash morphometry for eruption surveillance applications. *J Volcanol Geotherm Res* 297:11–27
- Liu EJ, Cashman KV, Rust AC (2015a) Optimizing shape analysis to quantify volcanic ash morphology. *Geo Res J* 8:14–30
- Liu EJ, Cashman KV, Rust AC, Gislason SR (2015b) The role of bubbles in generating fine ash during hydromagmatic eruptions. *Geology* 43(3):239–242

- Mangan MT, Cashman KV (1996) The structure of basaltic scoria and reticulite and inferences for vesiculation, foam formation, and fragmentation in lava fountains. *J Volcanol Geotherm Res* 73(1–2):1–18
- Maria A, Carey S (2002) Using fractal analysis to quantitatively characterize the shapes of volcanic particles. *J Geophys Res-Sol Ea* 107(B11):ECV 7-1–ECV 7-17
- Maria A, Carey S (2007) Quantitative discrimination of magma fragmentation and pyroclastic transport processes using the fractal spectrum technique. *J Volcanol Geotherm Res* 161(3):234–246
- Mastin LG, Guffanti M, Servranckx R, Webley P, Barsotti S, Dean K, Durant A, Ewert JW, Neri A, Rose WI, Schneider D, Siebert L, Stunder B, Swanson G, Tupper A, Volentik A, Waythomas CF (2009) A multidisciplinary effort to assign realistic source parameters to models of volcanic ash-cloud transport and dispersion during eruptions. *J Volcanol Geotherm Res* 186:10–21
- Mattsson HB, Hoskuldsson A (2011) Contemporaneous phreatomagmatic and effusive activity along the Hverfjall eruptive fissure, North Iceland: eruption chronology and resulting deposits. *J Volcanol Geotherm Res* 201(1–4):241–252
- Miwa T, Shimano T, Nishimura T (2015) Characterization of the luminance and shape of ash particles at Sakurajima volcano, Japan, using CCD camera images. *Bull Volcanol* 77(5):1–24
- Murtagh RM, White JDL (2013) Pyroclast characteristics of a subaqueous to emergent Surtseyan eruption, Black Point Volcano, California. *J Volcanol Geotherm Res* 267:75–91
- Nemeth K, Cronin SJ (2011) Drivers of explosivity and elevated hazard in basaltic fissure eruptions: the 1913 eruption of Ambrym Volcano, Vanuatu (SW-Pacific). *J Volcanol Geotherm Res* 201(1–4):194–209
- Oladottir BA, Sigmarsson O, Larsen G, Thordarson T (2008) Katla volcano, Iceland: magma composition, dynamics and eruption frequency as recorded by Holocene tephra layers. *Bull Volcanol* 70(4):475–493
- Oladottir BA, Sigmarsson O, Larsen G, Devidal JL (2011) Provenance of basaltic tephra from Vatnajökull subglacial volcanoes, Iceland, as determined by major- and trace-element analyses. *The Holocene* 21(7):1037–1048
- Owen J, Tuffen H, McGarvie DW (2013) Explosive subglacial rhyolitic eruptions in Iceland are fuelled by high magmatic H<sub>2</sub>O and closed-system degassing. *Geology* 41(2):251–254
- Parfitt EA, Wilson L (1995) Explosive volcanic eruptions (IX) the transition between Hawaiian-style lava fountaining and Strombolian explosive activity. *Geophys J Int* 121(1):226–232
- Particle Insight™ Website: <http://www.particulatesystems.com/products/particle-insight-dynamic-image-analyzer.aspx>
- Perugini D, Kueppers U (2012) Fractal analysis of experimentally generated pyroclasts: a tool for volcanic hazard assessment. *Acta Geophysica* 60(3):682–698
- Proussevitch AA, Mulukutla GK, Sahagian DL (2011) A new 3D method of measuring bubble size distributions from vesicle fragments preserved on surfaces of volcanic ash particles. *Geosphere* 7(1):62–69
- Riley CM, Rose WI, Bluth GJS (2003) Quantitative shape measurements of distal volcanic ash. *J Geophys Res-Sol Ea* 108(B10):2504. doi:10.1029/2001JB000818
- Schipper CI, White JDL (2016) Magma-slurry interaction in Surtseyan eruptions. *Geology* 44(3):195–198
- Schipper CI, White JDL, Houghton BF (2010) Syn- and post-fragmentation textures in submarine pyroclasts from Loihi Seamount, Hawaii. *J Volcanol Geotherm Res* 191(1–2):93–106
- Schipper CI, White JDL, Houghton BF (2011a) Textural, geochemical, and volatile evidence for a Strombolian-like eruption sequence at Lō’ihi Seamount, Hawaii. *J Volcanol Geotherm Res* 207(1–2):16–32
- Schipper CI, White JDL, Zimanowski B, Büttner R, Sonder I, Schmid A (2011b) Experimental interaction of magma and “dirty” coolants. *Earth Planet Sci Lett* 203:323–336
- Sheridan MF, Marshall JR (1983) Interpretation of pyroclast surface-features using SEM images. *J Volcanol Geotherm Res* 16(1–2):153–159
- Sigmarsson O, Vlastelic I, Andreasen R, Bindeman I, Devidal JL, Moune S, Keiding JK, Larsen G, Hoskuldsson A, Thordarson T (2011) Remobilization of silicic intrusion by mafic magmas during the 2010 Eyjafjallajökull eruption. *J Geophys Res-Sol Ea* 2(2):271–281
- Sigmarsson O, Haddadi B, Carn S, Moune S, Gudnason J, Yang K, Clarisse L (2013) The sulfur budget of the 2011 Grimsvotn eruption, Iceland. *Geophys Res Lett* 40(23):6095–6100
- Stovall WK, Houghton BF, Gonnermann H, Fagents SA, Swanson DA (2011) Eruption dynamics of Hawaiian-style fountains: the case study of episode 1 of the Kilauea Iki 1959 eruption. *Bull Volcanol* 73(5):511–529
- Wohletz KH (1983) Mechanisms of hydrovolcanic pyroclast formation—grain-size, scanning electron-microscopy, and experimental studies. *J Volcanol Geotherm Res* 17(1–4):31–63
- Zimanowski B, Büttner R, Lorenz V, Hafele HG (1997) Fragmentation of basaltic melt in the course of explosive volcanism. *J Geophys Res-Sol Ea* 102(B1):803–814